International Journal of Heat and Mass Transfer 52 (2009) 5381–5389

Contents lists available at ScienceDirect

International Journal of Heat and Mass Transfer

journal homepage: www.elsevier.com/locate/ijhmt

# 3D numerical simulation on shell-and-tube heat exchangers with middle-overlapped helical baffles and continuous baffles – Part II: Simulation results of periodic model and comparison between continuous and noncontinuous helical baffles

Jian-Fei Zhang, Ya-Ling He, Wen-Quan Tao *

*School of Energy and Power Engineering, Xi'an Jiaotong University, Xi'an 710049, China*

ARTICLE INFO

*Article history:*
Received 17 March 2009
Received in revised form 9 July 2009
Accepted 9 July 2009
Available online 18 August 2009

*Keywords:*
Heat exchangers
Helical baffles
Periodic model
Numerical simulation
Turbulence
Pressure drop
Heat transfer
Performance

ABSTRACT

In this paper, based on the simplified periodic model the performance predictions for heat exchanger with middle-overlapped helical baffles are carried out by 3D simulation for three different helix angles (30°, 40° and 50°), and the commercial codes of GAMBIT 2.3 and FLEUNT 6.3 are adopted in the simulation. It is found that the model average heat transfer coefficient per unit pressure drop of the 40° angle case is the largest, which is in qualitative agreement with the existing literature. The predicted average intersection angle of this case is the smallest, being consistent with the field synergy principle. The performance of periodic model with continuous helical baffle is also compared with that of the noncontinuous middle-overlapped helical baffles. It is found that the heat transfer coefficient per unit pressure drop of the noncontinuous middle-overlapped helical baffles is appreciably larger than that of the continuous helical baffle, indicating that the heat exchanger with noncontinuous middle-overlapped helical baffles has its advantage over the one with continuous helical baffle.



## 1. Introduction

The development of heat exchangers with high thermal efficiency is of great significance nowadays for the energy-saving purpose, because the operation of such equipment usually requires large amount of electricity. The required pumping power for operating a heat exchanger with higher thermal efficiency can be reduced. In the shell-and-tube heat exchangers (STHXs) it has long been recognized that the heat exchangers with helical baffles (STHXsHB) have a better performance than the conventional segmental baffles (STHXsSB) [1–8]. For example, in [8] a comprehensive comparison is provided from experimental data between the STHXsHB and STHXsSB. It is concluded that based on the same pumping power the STHXsHB can have appreciably better performance than that of STHXsSB. In order to further improve the thermal performance of the STHXsHB, numerical simulation can play an important role. However, limited by the present computer resource the simulation of the whole heat exchanger is still a very expensive task. In the companion paper [9] it has been demonstrated that for the STHXsHB fluid flow and heat transfer in the shell-side may very quickly reach their fully developed (or at least approximately fully developed) region, hence the periodic model based just on one cycle can be adopted without introducing significant error. Here by one cycle we mean the geometric unit within the space of one pitch [9]. In this paper simulation will be conducted by using the periodic model to investigate the effects of helical angle and helical structure on the thermal performance of STHXsHB.

## 2. Periodical model with noncontinuous baffles

Following assumptions are made in the present simulations: (1) the shell-side fluid is of constant thermal properties; (2) the fluid flow and heat transfer processes are turbulent and in steady-state; (3) the leak flows between tube and baffle and that between baffle and the shell are neglected; (4) the natural convection induced by the fluid density variation is neglected; (5) the tube wall temperatures are kept constant in the whole shell side; and (6) the heat exchanger is well-insulated hence the heat loss to the environment is totally neglected. For the readers' convenience, some parameter definitions of the noncontinuous helical baffles are shown in Fig. 1.

* Corresponding author.
*E-mail address:* wqtao@mail.xjtu.edu.cn (W.-Q. Tao).

0017-9310/$ - see front matter © 2009 Elsevier Ltd. All rights reserved.
doi:10.1016/j.ijheatmasstransfer.2009.07.007

**Nomenclatures**

| | |
|---|---|
| $A_o$ | heat exchange area based on the outer diameter of tube ($mm^2$) |
| $B$ | baffle spacing for segmental baffles or helical pitch for helical baffles (mm) |
| $c_p$ | specific heat (J/(kg K)) |
| $D_i$ | inside diameter of shell (mm) |
| $D_o$ | outside diameter of shell (mm) |
| $D_1$ | tube bundle-circumscribed circle diameter (mm) |
| $d_i$ | tube inner diameter (mm) |
| $d_o$ | outer diameter of tube (mm) |
| $h$ | heat transfer coefficient ($W\,(m^2\,K)^{-1}$) |
| $k$ | overall heat transfer coefficient ($W\,(m^2\,K)^{-1}$) |
| $l$ | effective length of tube (mm) |
| $M$ | mass flux (kg/s) |
| $N$ | tube number |
| $N_t$ | number of tube rows |
| $Nu$ | *Nu* number |
| $\Delta p$ | shell side pressure drop (kPa) |
| $q_s$ | volume flow rate ($m^3\,h^{-1}$) |
| $Re$ | *Re* number |
| $S$ | the cross-flow area at the shell centerline $(mm)^2$ |
| $\Delta t_m$ | logarithmic mean temperature difference (K) |
| $t$ | temperature (K) |
| $t_p$ | tube pitch (mm) |
| $u$ | fluid velocity in the shell side ($m\,s^{-1}$) |

*Greek symbols*

| | |
|---|---|
| $\alpha$ | intersection angle between velocity and temperature gradient |
| $\alpha_m$ | modulus average intersection angle |
| $\beta$ | helix angle |
| $\Phi$ | heat exchange quantity (W) |
| $\lambda$ | thermal conductivity $(W\,(m\,K)^{-1})$ |
| $v$ | kinematic viscosity of fluid ($m^2\,s^{-1}$) |
| $\Theta$ | dimensionless temperature |
| $\rho$ | density of fluid ($kg\,m^{-3}$) |

*Subscripts*

| | |
|---|---|
| in | inlet |
| out | outlet |
| s | shell side |
| t | tube side |
| w | wall |

### 2.1. Computational domain

The computational domain for the periodical model with 40° helix angle is shown in Fig. 2, and the geometry parameters for all periodical models are listed in Table 1.

### 2.2. Governing equations and boundary conditions

The governing equations for the mass, momentum and energy conservation and the turbulence model are the same as presented in Section 2.2 of the companion paper [9], and will be omitted here for simplicity. The wall surface boundary conditions for velocity and temperature are also the same. The major differences are in the periodic inlet and outlet boundary conditions, which are presented as follows.

The streamwise periodically fully-developed fluid flow and heat transfer has the following characteristics: [10–12]:

For fluid flow

$$u(x,y,z) = u(x,y,z+s) \tag{1}$$

$$v(x,y,z) = v(x,y,z+s) \tag{2}$$

$$w(x,y,z) = w(x,y,z+s) \tag{3}$$

$$p(x,y,z) - p(x,y,z+s) = p(x,y,z+s) - p(x,y,z+2s) \tag{4}$$

A suitable scaling of the fluid temperature for the periodically fully developed heat transfer with constant wall temperature is

$$\Theta(\vec{r}) = \frac{t(\vec{r}) - t_{\text{wall}}}{t_{\text{bulk,inlet}} - t_{\text{wall}}} \tag{5}$$

$$T_{\text{bulk,inlet}} = \left( \frac{\int_A T \left| \rho \vec{v} \cdot d\vec{A} \right|}{\int_A \left| \rho \vec{v} \cdot d\vec{A} \right|} \right)_{\text{inlet}} \tag{6}$$

where the integral is taken at the inlet section and scaled temperature, $\Theta$, obeys a periodic condition across the periodical domain as follows:

$$\Theta(\vec{r},0) = \Theta(\vec{r},L) \tag{7}$$

where $L$ is the length of one cycle.

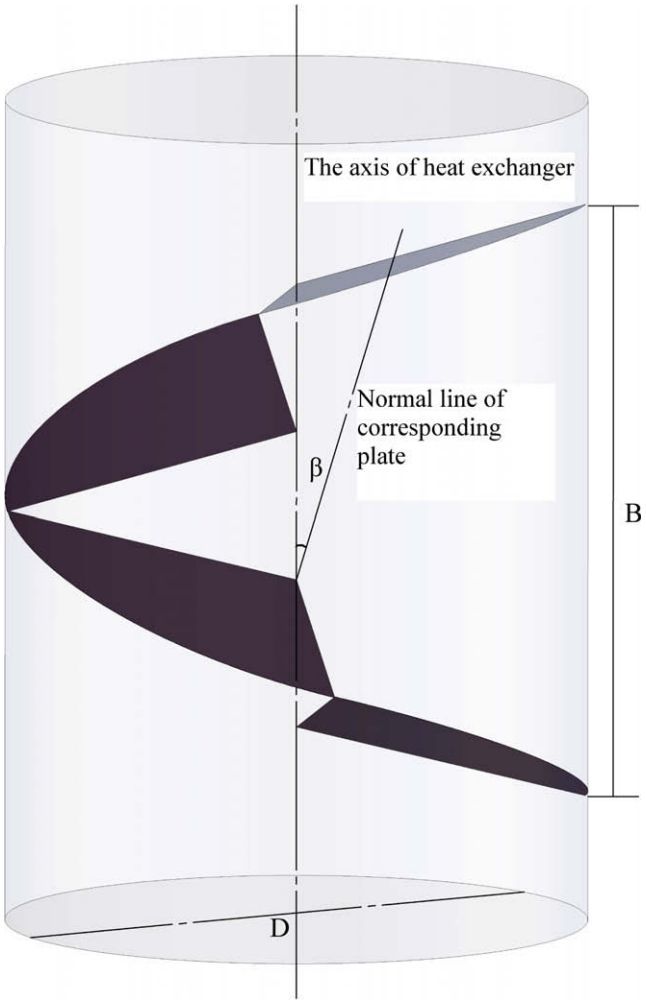


**Fig. 1.** Schematics of parameters definition.

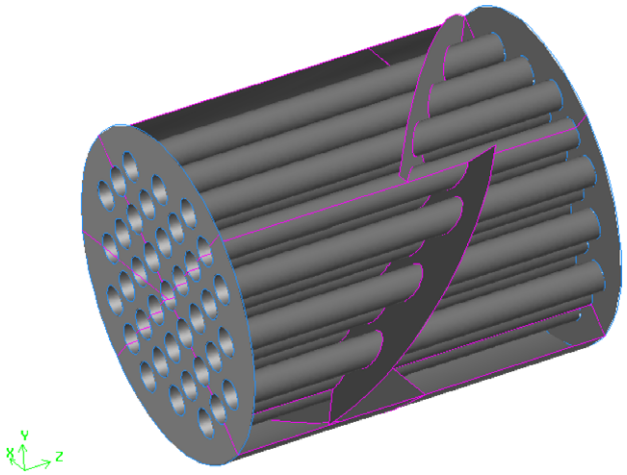

**Fig. 2.** Shaded partial scenograph of the periodical model with 40° helix angle.

**Table 1**
Geometry parameters for periodical models with noncontinuous baffles.

| Item | | Dimensions and description | | |
|---|---|---|---|---|
| Shell side parameters | $D_o/D_i$/mm | 223/211 | 223/211 | 223/211 |
| | Material | 0Cr18Ni9 | 0Cr18Ni9 | 0Cr18Ni9 |
| Tube parameters | $d_o/d_i$/mm | 19/15 | 19/15 | 19/15 |
| | Effective length/mm | 168 | 250 | 349 |
| | Number | 37 | 37 | 37 |
| | Layout pattern | 45° | 45° | 45° |
| | Tube pitch/mm | 25 | 25 | 25 |
| | Material | 0Cr18Ni9 | 0Cr18Ni9 | 0Cr18Ni9 |
| Baffle parameters | Baffle pitch/mm | 168 | 250 | 349 |
| | Helix angle | 30° | 40° | 50° |
| | Thickness/mm | 3 | 3 | 3 |

The temperature of tube walls is set as constant (300 K) and the upstream bulk temperature is set as 350 K. The shell wall of the model is assumed to be adiabatic. Heat conduction of baffles in heat exchanger is considered by using the shell conduction in thin-walls model [13] in FLUENT. The baffles thermal conductivity and the thermophysical properties of the oil are the same as in the previous simulation [9].

### 2.3. Grid generation and numerical method

The 3D grid system was established using the commercial code GAMBIT based on the 3D geometry created in a commercial CAD program. The computational domain is meshed with unstructured tetrahedral elements. In the regions adjacent to the tubes much finer grid distribution is used. Grid independence tests are carried out for every model. For example, three different grid systems with 13,65,821, 19,22,792 and 23,90,949 cells are adopted for the calculation of model with 40° helix angle, and the difference in pressure drop and heat transfer coefficient between the last two grid systems are around 2%. Thus, considering both the computational cost and solution precisions the second grid system is taken for the computational model. The cells number of the grid system for models with 30° and 50° helix angles are 1337,125, and 2726,341, respectively. The meshed computational periodical model with 40° helix angle is shown in Fig. 3.

The commercial code FLUENT is adopted to calculate the flow and heat transfer in the computational domain. The adopted numerical methods are the same as presented in Section 2.3 of the companion paper [9]. A parallel computation is performed on a DELL workstation with two Quad-Core CPUs and 4 GB memory by using FLUENT and every simulation case takes approximately 24 h to get a converged solution compared with 72 h for the whole heat exchanger simulation [9].

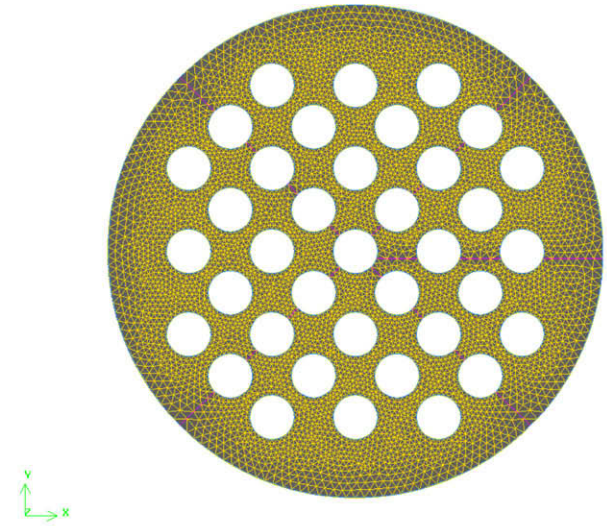

(a) Front view of grid for periodical model with noncontinuous baffles at 40° helix angle

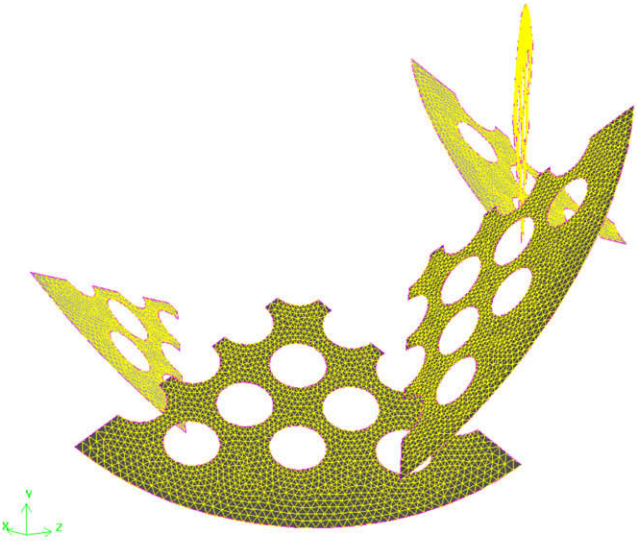

(b) Grid of periodical model with noncontinuous baffles at 40° helix angle

**Fig. 3.** Meshes of periodical model with noncontinuous baffles at 40° helix angle.

### 2.4. Data reduction

For the readers' convenience the major equations used in the data reduction are collected as follows:

$$u = \frac{q_s}{S} \tag{8}$$

$$S = 0.5B\left[D_i - D_1 + \frac{D_1 - d_o}{t_p}(t_p - d_o)\right] \tag{9}$$

$$B = \sqrt{2}D_i \cdot \tan\beta \tag{10}$$

$$Re_s = \frac{ud_o}{v_s} \tag{11}$$

$$\Phi_s = M_s \times c_{ps} \times (t_{s,in} - t_{s,out}) \tag{12}$$

$$h_s = \frac{\Phi_s}{A_o \cdot \Delta t_m} \tag{13}$$

$$A_o = N_t \cdot \pi d_o l \tag{14}$$

$$\Delta t_m = \frac{\Delta t_{max} - \Delta t_{min}}{\ln(\Delta t_{max}/\Delta t_{min})} \tag{15}$$

$$\Delta t_{max} = t_{s,in} - t_w \tag{16}$$

$$\Delta t_{min} = t_{s,out} - t_w \tag{17}$$

$$Nu_s = \frac{h_s d_o}{\lambda_s} \tag{18}$$

For the meanings of above quantities, the nomenclature may be consulted.

## 3. Results and discussion for model with noncontinuous baffles

### 3.1. Effect of the helix angle on performance

The path lines in the shell side of heat exchanger with 40° helix angle are shown in Fig. 4. It can be clearly observed that the fluid passes though the tube bundles in a helical pattern.

The variation trends of pressure drops with mass flow rate are shown in Fig. 5. It can be seen that at the same mass flow rate and shell inner diameter, the pressure drop decreases with the increasing of helix angel. Even though the flow path of one cycle with bigger helical angle is longer than that of a smaller angle, the overall pressure drop of the bigger angle case is still less than that of the smaller angle because of in the later case fluid flows in a much smoother manner for which the limiting case of $\beta = 90°$ is the parallel flow. The pressure drop decrease trend becomes mild after the helical angle reaches 40°. It may be worth noting that for the total pressure drop between inlet and outlet of the tested heat exchanger is in the order of 20–50 kPa as indicated in Fig. 5 of the companion paper [9]. While the pressure drop in each of the cycles predicted here is about 140 Pa. There are six cycles in the simulated exchanger, so overall pressure drop will be about 840 Pa, which differs from the overall test data very much. This great difference can be explained by the huge pressure drop at the inlet and out let of the tested heat exchanger. Our computational model comes from an experiment tested unit, and the nozzles diameter (30 mm) of it is too small compared to the TEMA standard, so the pressure drop of each cycle in tube bundle zone is much small than the pressure drop in the inlet and outlet section and the pressure drop caused by the nozzles. According to Gaddis and Gnielinski [14], the pressure drop in the inlet and outlet nozzles can be predicted by $\Delta P_{nozzle} = \xi \times 0.5 \times \rho v^2_{nozzle}$, where $\xi$ is taken as 1.5 or 2.0, so the pressure drop of the nozzles for 3.5 kg/s flow rate is predicted to be around 22.3 kPa if $\xi$ is taken as 1.5. This estimation is quite consistent with our test result.

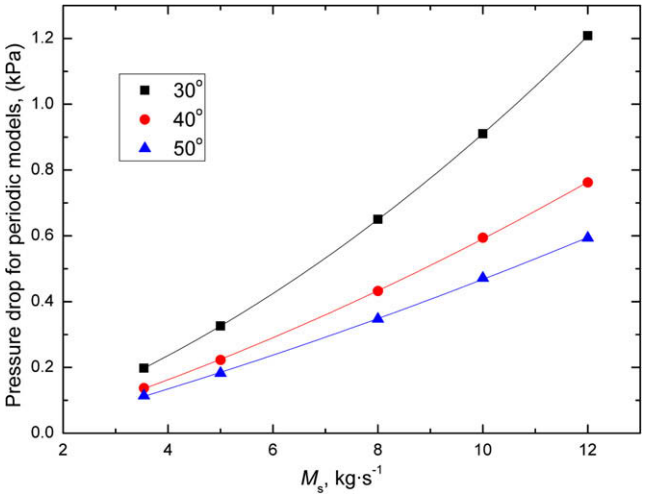


**Fig. 5.** Pressure drop versus shell side mass flow rate for the periodical models with noncontinuous baffles at different helix angles.

Fig. 6 provides the comparison of shell side heat transfer coefficient among three periodical models within the range of mass flow rate tested. The results show that the heat transfer coefficient increases with the decrease of the helix angle. This variation trend can be understood from two aspects. First, at fixed shell inner diameter, the helix pitch $B$ and the cross-flow area $S$ decrease with the decrease of helix angle (Eqs. (9) and (10)), and at same mass flow rate the shell side velocity increases with the decrease of cross-flow area (Eq. (8)). Thus the convective heat transfer is enhanced with the decrease of the helical angle because of the increased velocity. Second, with the decrease of the helical angle, the flow pattern of shell-side fluid flow gradually approaches the external flow cross a tube bank, which has better heat transfer intensity than the flow parallel to a tube bank at the same fluid velocity [15]. Again, it is to be noticed that the heat transfer

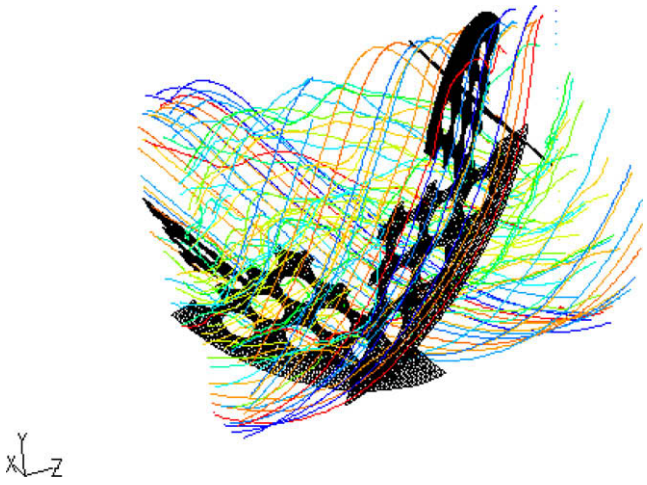

**Fig. 4.** Path lines in the periodical model with noncontinuous baffles at 40° helix angle ($M_s$ = 8 kg/s).

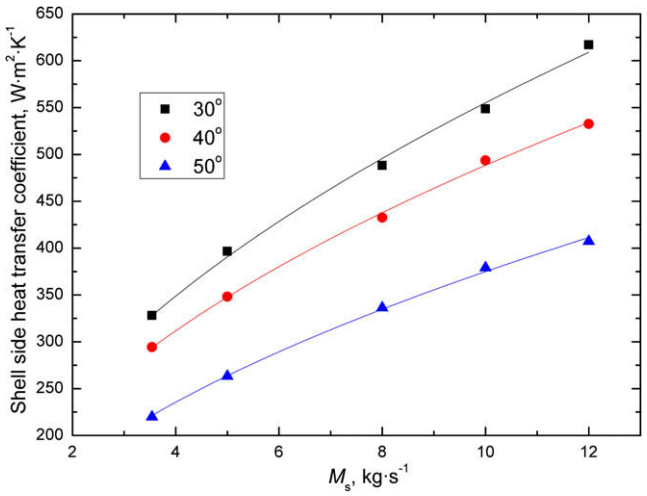


**Fig. 6.** Shell side heat transfer coefficient versus volume flow rate for the periodical models with noncontinuous baffles at different helix angles.

increase trend with the decrease in the helical angle becomes mild after the helical angle reaches 40°.

The variation trends of *Nu* with $Re_s$ for each model are shown in Fig. 7 with log–log coordinates. Among all the three models the *Nu* number of helical baffle with 40° is the highest. This result is in qualitative agreement with the results provided in the literature [1–3].

Comparisons of heat transfer coefficient per unit pressure drop of each model are given in Fig. 8. It can be obviously observed that 40° is the optimum helix angle at which the comprehensive performance is the best.

### 3.2. Field synergy principle analysis

In 1998, Guo and his co-workers proposed a novel concept for enhancing convective heat transfer of parabolic flow [16–18]: the reduction of the intersection angle between velocity and temperature gradient can effectively enhance convective heat transfer. Later this concept has been enhanced in different aspects [19–25]. For the readers' convenience the basic idea of the filed synergy principle is briefly reviewed here [16]. For two-dimensional (2D) boundary layer flow and heat transfer along a plate with a temperature different from the oncoming flow, the energy equation takes following form:

$$\rho c_p\left(u\frac{\partial t}{\partial x}+v\frac{\partial t}{\partial y}\right)=\frac{\partial}{\partial y}\left(k\frac{\partial t}{\partial y}\right) \tag{19}$$

Integrating above equation along the thermal boundary layer and notice that at the outer edge of the thermal boundary layer $\partial t/\partial y = 0$, we have

$$\rho c_p\int_0^{\delta_t}\left(\vec{U}\cdot\mathrm{grad}t\right)dy=-\left(\lambda\frac{\partial t}{\partial y}\right)_{y=0}=q_w \tag{20}$$

The convective term has been transformed to the dot product form of the velocity vector and the temperature gradient, and the right-hand side is the heat flux between the solid wall and the fluid, i.e., the convective heat transfer rate per unit area. The dot product $(\vec{U}\times\mathrm{grad}t)=|\vec{U}||\mathrm{grad}T|\cos\alpha$, where $\alpha$ is the intersection angle between velocity and temperature gradient. It is obvious that for a fixed flow rate and temperature difference, the smaller the intersection angle between the velocity and the temperature gradient, the larger the heat transfer rate.

From the above brief review it can be seen that the local intersection angle between velocity and temperature gradient is an indication of heat transfer intensity. In order to get an averaged intersection angle of the computational domain, different definitions may be used. It has been demonstrated in [26,27] that except the simple arithmetic average method different definitions only differ in the absolute values of the angle, and as far as the variation trend of the angle with fluid velocity (or Reynolds number) is concerned the trends of different definitions are qualitatively the same. When the relation between the intersection angle and the fluid velocity is concerned, it is the trend rather than the absolute value that is of significance. In this paper following modulus averaged definition is adopted [26,27]:

$$\alpha_m=\sum\left[\frac{(|\vec{u}|_i\times|\mathrm{grad}t|_i)dV_i}{\sum(|\vec{u}|_i\times|\mathrm{grad}t|_i)dV_i}\right]\alpha_i \tag{21}$$

The modulus average intersection angles are calculated by a self-developed UDF program in conjunction with FLUENT. The predicted relationship of $\alpha_m$ versus *Re* number is presented in Fig. 9. The numerical results shown in the figure demonstrate that the configuration with higher heat transfer rate has the smaller modulus

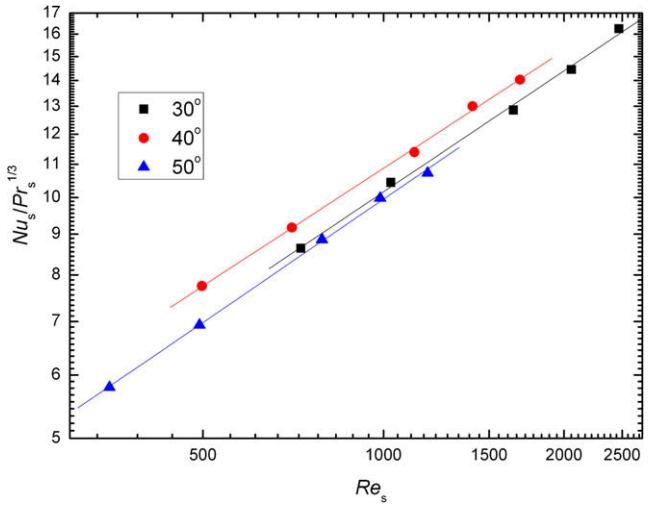


**Fig. 7.** *Nu* number versus *Re* number for the periodical models with noncontinuous baffles at different helix angles.

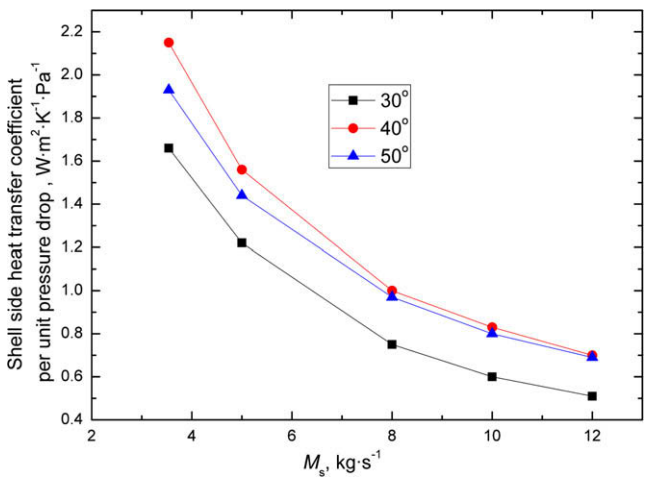


**Fig. 8.** Shell side heat transfer coefficient per unit pressure drop versus mass flow rate for the periodical models with noncontinuous baffles at different helix angles.

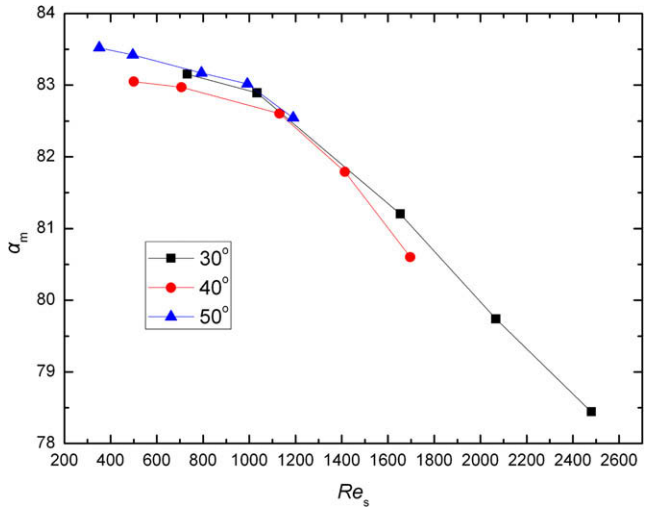


**Fig. 9.** Modulus average intersection angle versus *Re* number for the periodical models with noncontinuous baffles at different helix angles.

average intersection angle between velocity and temperature gradient, which is very consistent with the field synergy principle.

## 4. Periodical model with continuous baffle

In this section, the comparison between the model with continuous baffle and noncontinuous baffle model at optimum helix angle of 40° will be discussed.

### 4.1. Computational domain

The computational domain of a periodical model with continuous baffle at 40° helix angle is shown in Fig. 10. All the geometry parameters for the continuous periodical model are listed in Table 2.

### 4.2. Governing equations and boundary conditions

The governing equations and boundary conditions for the periodical model with continuous baffle are the same as that for periodical model with noncontinuous baffles.

### 4.3. Grid generation and numerical method

The computational model is meshed with unstructured tetrahedral elements by commercial code GAMBIT and the region adjacent to the tubes is meshed much finer. The meshes of computational model are shown in Fig. 11. Grid independence tests are carried out for this model. Three different grid system with 2910,031, 4528,336 and 5392,852 cells are adopted for the calculation of the model, and the difference in pressure drop and heat transfer coefficient between last two grid systems are around 2%, thus, considering both the computational source and solution precisions the second grid system is taken for the computational model.

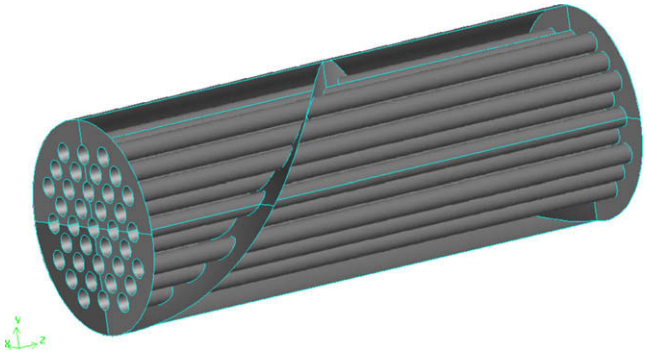

**Fig. 10.** Shaded partial scenograph of the periodical model with continuous baffle at 40° helix angle.

**Table 2**
Geometry parameters for periodical model with continuous baffle.

| Item | | Dimensions and description |
|---|---|---|
| Shell side parameters | $D_o/D_i$/mm | 223/211 |
| | Material | 0Cr18Ni9 |
| Tube parameters | $d_o/d_i$/mm | 19/15 |
| | Effective length/mm | 556 |
| | Number | 37 |
| | Layout pattern | 45° |
| | Tube pitch/mm | 25 |
| | Material | 0Cr18Ni9 |
| Baffle parameters | Baffle pitch/mm | 556 |
| | Helix angle | 40° |
| | Thickness/mm | 3 |

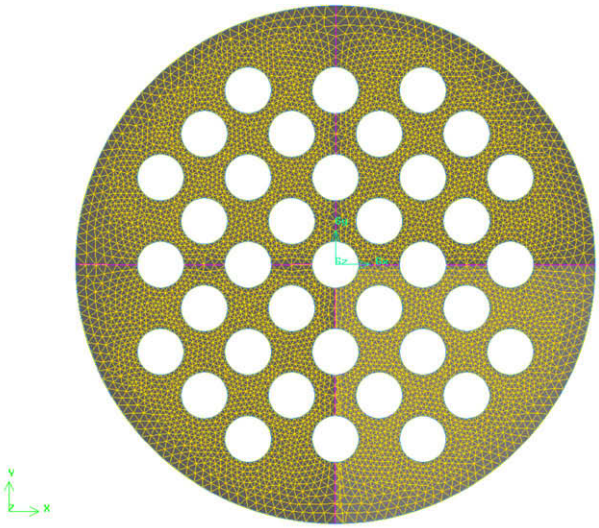

(c) Front view of grid

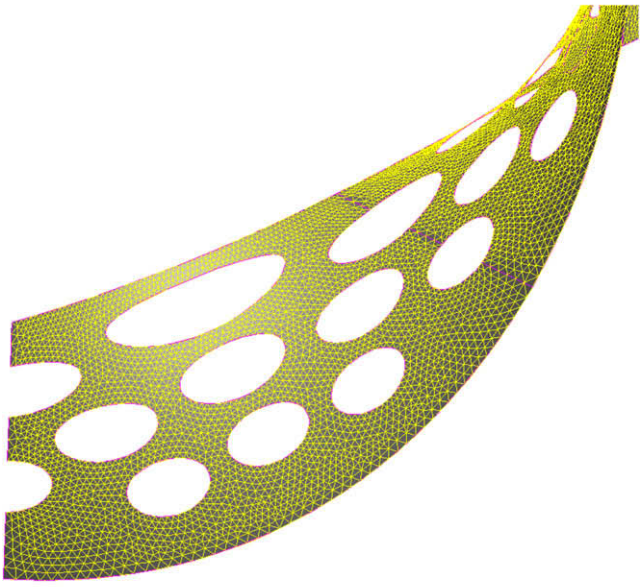

(c) Local grid of continuous baffle

**Fig. 11.** Meshes of the periodical model with continuous baffle at 40° helix angle.

The details of numerical methods and computational techniques are the same as for the noncontinuous model. For every simulation case it takes approximately 24 h to get converged solution.

### 4.4. Data reduction

The helical pitch is determined as follows:

$$B = \pi D_i \cdot \tan\beta \tag{22}$$

The determinations of shell side velocity, *Re* number and *Nu* number for the periodical model are the same as that for whole heat exchanger and periodical models with noncontinuous baffles.

### 4.5. Results and performance comparison

The path lines in the shell side of the model with continuous baffle are shown in Fig. 12. It can be seen that the fluid passes

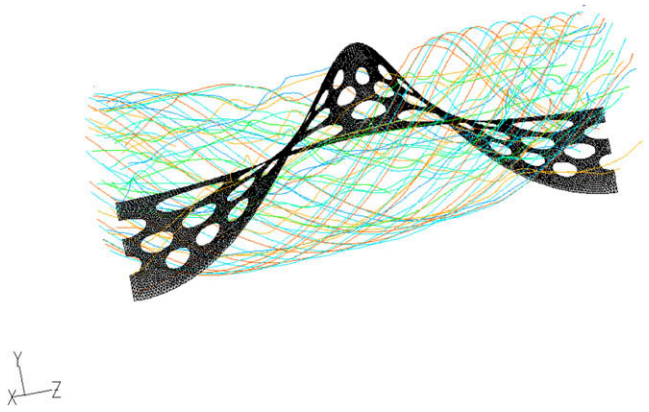


**Fig. 12.** Path lines in the periodic model with continuous baffle at 40° helix angle ($M_s$ = 8 kg/s).

though the tube bundles in a helical pattern. From Figs. 11(c) and 12 it can be clearly observed that in the continuous helical baffle the holes through which tubes are going have different outlines and sizes because of the continuous helical requirement. And this is the point that the continuous helical baffle provides much more difficulty in manufacturing process.

The variation trends of pressure drops along mass flow rate are shown in Fig. 13. The pressure drop of model with continuous baffle is 31–46% higher than that of model with the noncontinuous baffles. It is worth noting that at the same helical angle the continuous baffle has much longer pitch than that of the middle-overlapped helical baffles (556 versus 250, see Tables 1 and 2). Therefore another comparison is made for pressure gradient versus mass flow rate, which is shown in Fig. 14. As can be seen there in this comparison frame, the pressure gradient of the continuous baffle is about 35–42% lower than that of the noncontinuous baffle.

Fig. 15 illustrates the comparison of shell side heat transfer coefficient versus mass flow rate. The results show that the heat transfer coefficient of the periodic model with continuous baffle is lower than that of the periodic model with noncontinuous baffles. The enhancement of heat transfer for the noncontinuous case can be understood from following two aspects. First, at fixed shell inner diameter, the helix pitch $B$ of the periodic model with continuous baffle is larger than that of the periodic model with noncontinuous baffles (Eqs. (10) and (22)), so at same mass flow rate the

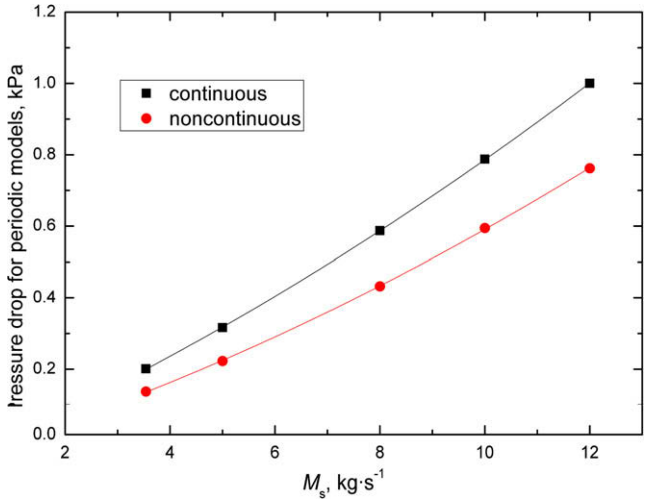


**Fig. 13.** Pressure drop versus shell side mass flow rate for periodic models with different baffle types at 40° helix angle.

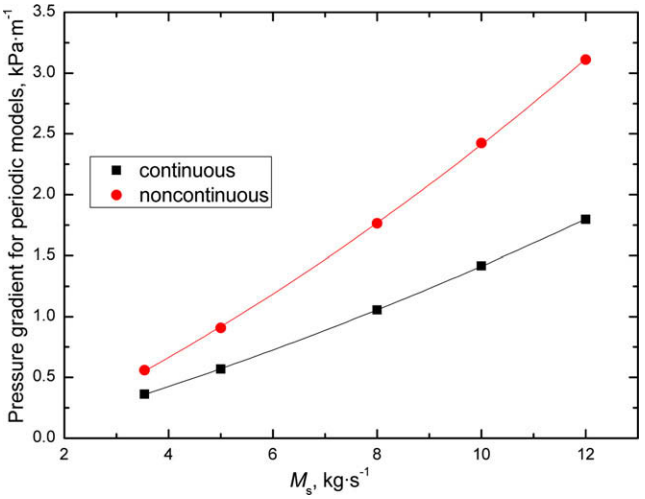


**Fig. 14.** Pressure gradient versus shell side mass flow rate for periodic models with different baffle types at 40° helix angle.

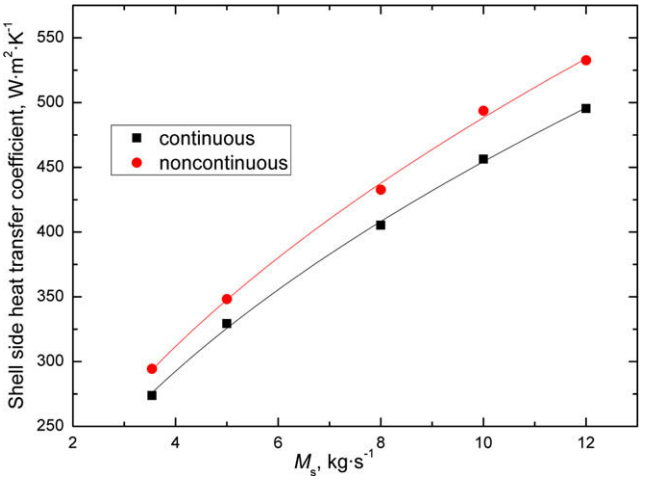


**Fig. 15.** Shell side heat transfer coefficient versus mass flow rate for periodic models with different baffle types at 40° helix angle.

shell side velocity of the continuous baffle case decreases due to the increase of cross-flow area (Eqs. (8) and (9)). Second, for the continuous baffle case the shell-side fluid flows in a smoother manner than that in noncontinuous baffle case, which in tern leads to less disturbances in the shell-side fluid.

In Fig. 16 the variation trends of $Nu$ versus $Re_s$ are presented. The $Nu$ number of the continuous baffle model is around 40% higher than that of model with the noncontinuous baffles. It should be emphasized that this result is not confronted with the heat transfer coefficient versus mass flow rate shown in Fig. 15. As indicated above at the same mass flow rate, the fluid velocity of the continuous model is much less than the noncontinuous model, hence the Reynolds number of the continuous model is much less than that of the noncontinuous one, leading to a significant increase in Nusselt number of the continuous model at the same Reynolds number.

Comparisons of heat transfer coefficient per unit pressure drop of the two models are given in Fig. 17. It can be obviously observed that model with the noncontinuous baffles has better comprehensive performance than that of model with continuous baffle. If

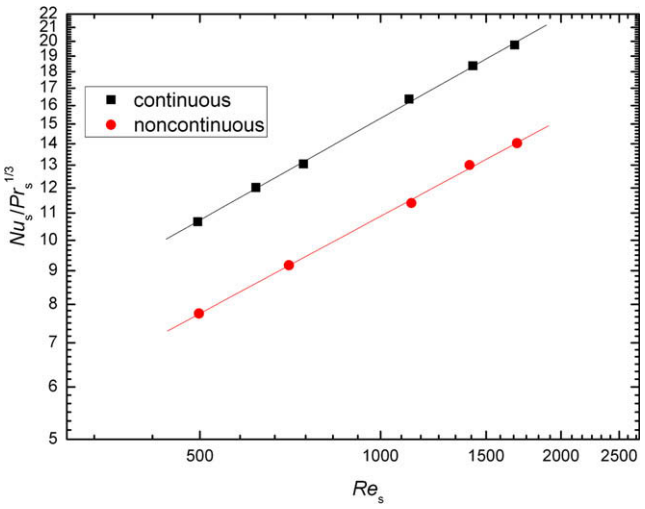


**Fig. 16.** *Nu* number versus *Re* number for periodic models with different baffle types at 40° helix angle.

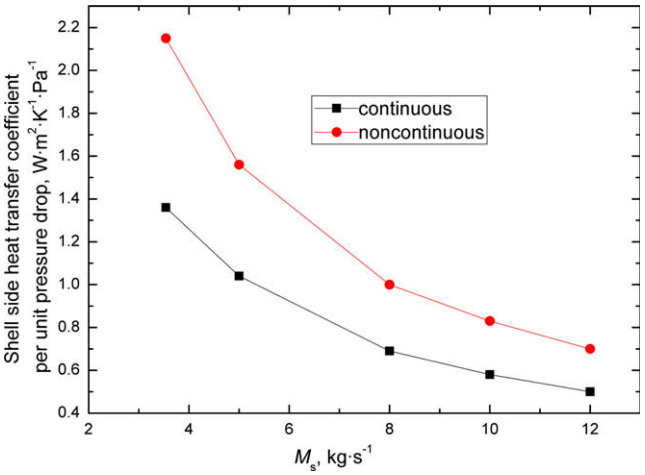


**Fig. 17.** Shell side heat transfer coefficient per unit pressure drop versus mass flow rate for periodic models with different baffle types at 40° helix angle.

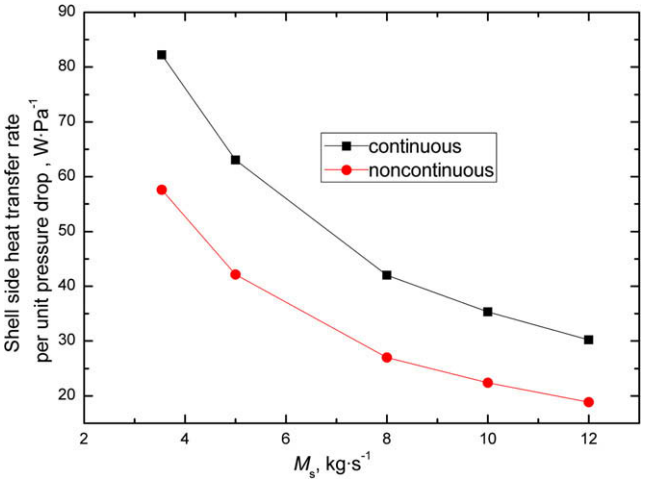


**Fig. 18.** Shell side heat transfer rate per unit pressure versus mass flow rate for periodic models with different baffle types at 40° helix angle.

based on the transfer rate per unit pressure drop, we have the results shown in Fig. 18. It can be seen that the heat transfer rate per unit pressure gradient of the continuous baffle is about 43–60% higher than that of the noncontinuous baffle.

For a fixed thermal load and allowed pressure drop, the heat transfer coefficient per unit pressure drop is the most meaningful comparison criterion. Thus from above comparison it is seemingly that the usage of continuous baffle does not provide attractive advantage in its thermal performance apart from its complicated manufacturing process.

## 5. Conclusion

3D simulation on three periodic models with middle-overlapped helical baffles at different helix angles are carried out, and the effects of helix angle on the performance of STHXsHB are investigated based on the simulation results. In addition, the performance of periodic model with continuous helical baffle is compared with that of periodic model with noncontinuous middle-overlapped helical baffles at optimum helix angle of 40°. The major conclusions are as follows.

(1) It is found that the periodic model with 40° helix angle possesses the best performance among all, which is in qualitative agreement with the results provided in the literature [1–3,8]. And the cycle average intersection angle between velocity and temperature gradient for 40° helix angle case is the smallest which is consistent with the field synergy principle.

(2) It is found that at same volume flow the heat transfer coefficient per unit pressure drop of the noncontinuous middle-overlapped helix angle case is larger than that of the continuous helix angle case. Since for the fixed thermal load and allowed pressure drop condition, the heat transfer coefficient per unit pressure drop is the most meaningful comparison criterion, it is seemingly that the continuous helical baffle does not have attractive advantage for the engineering applications.

## Acknowledgments

This work is supported by the National Fundamental Research Program of China (973 Program) (2007CB206902), the Key Project of Chinese Ministry of Education (No. 306014) and the Key Project of National Natural Science Foundation of China (No. 50636050).

## References

[1] J. Lutcha, J. Nemcansky, Performance improvement of tubular heat exchangers by helical baffles, Trans. Inst. Chem. Eng. 68 (1990) 263–270.
[2] P. Stehlik, J. Nemcansky, D. Kral, Comparison of correction factors for shell-and-tube heat exchangers with segmental or helical baffles, Heat Transfer Eng. 15 (1) (1994) 55–65.
[3] D. Kral, P. Stelik, H.J. Van Der Ploeg, Bashir I. Masster, Helical baffles in shell-and-tube heat exchangers. Part 1: experimental verification, Heat Transfer Eng. 17 (1) (1996) 93–101.
[4] S.L. Wang, Hydrodynamic studies on heat exchangers with helical baffles, Heat Transfer Eng. 23 (3) (2002) 43–49.
[5] Z.G. Zhang, T. Xu, X.M. Fang, Experimental study on heat transfer enhancement of a helically baffled heat exchanger combined with three-dimensional finned tubes, Appl. Therm. Eng. 24 (14–15) (2004) 2293–2300.
[6] B. Peng, Q.W. Wang, C. Zhang, G.N. Xie, L.Q. Luo, Q.Y. Chen, M. Zeng, An experimental study of shell-and-tube heat exchangers with continuous helical baffles, ASME J. Heat Transfer 129 (2007) 1425–1431.
[7] Yong-Gang Lei, Ya-Ling He, Pan Chu, Rui Li, Design and optimization of heat exchangers with helical baffles, Chem. Eng. Sci. 63 (2008) 4386–4395.
[8] Jian-Fei Zhang, Bin Li, Wen-Jiang Huang, Yong-Gang Lei, Ya-Ling He, Wen-Quan Tao, Experimental performance comparison of shell side heat transfer for shell-and-tube heat exchangers with middle-overlapped helical baffles and segmental baffles, Chem. Eng. Sci. 64 (2009) 1643–1653.

[9] Jian-Fei Zhang, Ya-Ling He, Wen-Quan Tao, 3D Numerical simulation on shell-and-tube heat exchangers with middle-overlapped helical baffles and continuous baffles. Part I: numerical model and results of whole heat exchanger with middle-overlapped helical baffles, Int. J. Heat Mass Transfer 52 (2009) 5371–5380.
[10] S.V. Patankar, C.H. Liu, E.M. Sparrow, Fully developed flow and heat transfer in ducts having streamwise-periodic variations of cross-sectional area, ASME J. Heat Transfer 99 (1977) 180–186.
[11] W.Q. Tao, Numerical Heat Transfer, second ed., Xi'an Jiaotong University Press, Xi'an, China, 2001. pp. 488–490.
[12] L. Gong, Z.Y. Li, Y.L. He, W.Q. Tao, Discussion on numerical treatment of periodic boundary condition for temperature, Numer. Heat Transfer B 52 (5) (2007) 429–0448.
[13] FLUENT 6.3: User's Guide, FLUENT Inc., 2006, Section 7.13.1.
[14] E.S. Gaddis, V. Gnielinski, Pressure drop on the shell side of shell-and-tube heat exchangers with segmental baffles, Chem. Eng. Process. 36 (2) (1997) 149–159.
[15] S.M. Yang, W.Q. Tao, Heat Transfer, third ed., High Education Press, Beijing, China, 1998. pp. 175–178.
[16] Z.Y. Guo, D.Y. Li, B.X. Wang, A novel concept for convective heat transfer enhancement, Int. J. Heat Mass Transfer 41 (1998) 2221–2225.
[17] S. Wang, Z.X. Li, Z.Y. Guo, Novel concept and device of heat transfer augmentation, in: Proceedings of 11th International Heat Transfer Conference, vol. 5, 1998, pp. 405–408.
[18] Z.Y. Guo, S. Wang, Novel concept and approaches of heat transfer enhancement, in: P. Cheng et al. (Eds.), Proceedings of Symposium on Energy Engineering in the 21th Century, vol. 1, Begell House, New York, 2000, pp. 118–126.
[19] B. Hua, P.S. Guo, S.S. Lu, et al. The study of field synergy theory in transfer process, in: Proceeding of 2001 IAMS International Seminar on Materials for Use in Lithium Battery and Transport Phenomena in Material Processing, Japan, November 2001, pp. 26–27.
[20] W.Q. Tao, Z.Y. Guo, B.X. Wang, Field synergy principle for enhancing convective heat transfer – its extension and numerical verifications, Int. J. Heat Mass Transfer 45 (2002) 3849–3856.
[21] W.Q. Tao, Y.L. He, Q.W. Wang, et al., A unified analysis on enhancing single phase convective heat transfer with field synergy principle, Int. J. Heat Mass Transfer 45 (2002) 4871–4879.
[22] S. Shen, W. Liu, W.Q. Tao, A unified analysis on enhancing single phase convective heat transfer with field synergy principle, Int. J. Heat Mass Transfer 45 (2002) 4871–4879.
[23] Y.P. Cheng, Z.G. Qu, W.Q. Tao, et al., Numerical design of efficient slotted fin surface based on the field synergy principle, Numer. Heat Transfer A 45 (6) (2004) 517–538.
[24] Y.L. He, M. Wu, W.Q. Tao, et al., Improvement of the thermal performance of pulse tube refrigerator by using a general principle for enhancing energy transport and conversion processes, Appl. Therm. Eng. 24 (2004) 79–93.
[25] Z.Y. Guo, W.Q. Tao, R.K. Shah, The field synergy (coordination) principle and its applications in enhancing single phase convective heat transfer, Int. J. Heat Mass Transfer 48 (2005) 1797–1807.
[26] J.J. Zhou, Research on the Mechanisms of HT Enhancement and Saving Energy or Compact HEx Surface and Its Optimization, Ph.D. dissertation, Xi'an Jiaotong University, Xi'an, China, 2005.
[27] J.J. Zhou, W.Q. Tao, Three-dimensional numerical simulation and analysis of the airside performance of slotted fin surfaces with radial strips, Eng. Comput. 22 (7–8) (2005) 940–957.